Three-dimensional virtual histology of the human hippocampus based on phase-contrast computed tomography

Marina Eckermann[a,b], Bernhard Schmitzer[c], Franziska van der Meer[d,1], Jonas Franz[d,e,f], Ove Hansen[a], Christine Stadelmann[b,d], and Tim Salditt[a,b,2]

[a]Institut für Röntgenphysik, Universität Göttingen, 37077 Göttingen, Deutschland; [b]Cluster of Excellence "Multiscale Bioimaging: from Molecular Machines to Networks of Excitable Cells," Universität Göttingen, 37077 Göttingen, Deutschland; [c]Institut für Informatik, Universität Göttingen, 37077 Göttingen, Deutschland; [d]Institut für Neuropathologie, Universitätsmedizin Göttingen, 37099 Göttingen, Deutschland; [e]"Campus Institut für Dynamik Biologischer Netzwerke," Universität Göttingen, 37075 Göttingen, Deutschland; and [f]Max-Planck-Institut für Experimentelle Medizin, 37075 Göttingen, Deutschland

Edited by Marcus E. Raichle, Washington University in St. Louis, St. Louis, MO, and approved October 20, 2021 (received for review July 30, 2021)

We have studied the three-dimensional (3D) cytoarchitecture of the human hippocampus in neuropathologically healthy and Alzheimer's disease (AD) individuals, based on phase-contrast X-ray computed tomography of postmortem human tissue punch biopsies. In view of recent findings suggesting a nuclear origin of AD, we target in particular the nuclear structure of the dentate gyrus (DG) granule cells. Tissue samples of 20 individuals were scanned and evaluated using a highly automated approach of measurement and analysis, combining multiscale recordings, optimized phase retrieval, segmentation by machine learning, representation of structural properties in a feature space, and classification based on the theory of optimal transport. Accordingly, we find that the prototypical transformation between a structure representing healthy granule cells and the pathological state involves a decrease in the volume of granule cell nuclei, as well as an increase in the electron density and its spatial heterogeneity. The latter can be explained by a higher ratio of heterochromatin to euchromatin. Similarly, many other structural properties can be derived from the data, reflecting both the natural polydispersity of the hippocampal cytoarchitecture between different individuals in the physiological context and the structural effects associated with AD pathology.

X-ray phase-contrast tomography | multiscale imaging | human hippocampus | 3D virtual histology | Alzheimer's disease

Brain mappings of the cyto- and myeloarchitecture in larger brain areas performed postmortem are required to advance our understanding of the human brain in quantitative terms. Beyond refinements of a brain atlas, they are also essential for later integration of in vivo functional observations with high-resolution structural data (1–3). Mapping the brain, however, requires additional imaging approaches, which can visualize and quantify the three-dimensional (3D) architectonics, including data from more than a single individual (2). The potential of phase-contrast X-ray tomography also known as phase-contrast computed tomography (PC-CT) for 3D brain imaging has been recently demonstrated, both for small animals models (4–8) and the human brain (9–12). Since the entire 3D architecture on all scales is relevant for physiological functions and pathological mechanisms, multiscale implementations of PC-CT (13) are particularly suitable for brain mapping.

Complementary to genomics, proteomics, and metabolics, structural data are also required to unravel mechanisms of neurodegenerative diseases. Such data must be comprehensive (large patient and control groups), quantitative, and fully digital; amenable to advanced analysis including deep learning; and intrinsically three-dimensional. Alzheimer's disease (AD) is a case in point: Evidence for morphological changes in the hippocampus upon aging and disease can be found already in vivo with MRI. To interpret such data based on a reference model, a 3D probabilistic atlas of the hippocampus was put forward in ref. 3, combining postmortem MRI with histology. The authors concluded that, to test the hypothesis of differential involvement of hippocampal subfields in AD, a "more granular study" of the hippocampus in aging and disease would be required and hence higher-resolution and truly 3D data.

To this end, we here present an advanced and multiscale implementation of PC-CT in combination with automated segmentation and statistical analysis of morphological features. In this way, a much-needed complement to conventional 2D histology is provided, sparing sample sectioning and staining. The signal is generated by the spatial variation of the real-valued part of the X-ray index of refraction $n = 1 - \delta + i\beta$, with δ being proportional to the electron density. Importantly, the advantage of PC-CT derives from the real-valued decrement being significantly larger than the imaginary, absorption-accounting component β; i.e., $\delta/\beta \approx 10^3$ in the hard X-ray regime. Image contrast is then efficiently formed by free-space propagation, i.e., self-interference of a partially coherent beam behind the object. The

Significance

We demonstrate multiscale phase-contrast X-ray computed tomography (CT) of postmortem human brain tissue. Large tissue volumes can be covered by parallel-beam CT and combined with subcellular detail for selected regions scanned at high magnification. This has been repeated identically for a larger number of individuals, including both Alzheimer's-diseased patients and a control group. Optimized phase retrieval, followed by automated segmentation based on machine learning, as well as feature identification and classification based on optimal transport theory, indicates a pathway from healthy to pathological structure without prior hypothesis. This study provides a blueprint for studying the cytoarchitecture of the human brain and its alterations associated with neurodegenerative diseases.

Author contributions: M.E., C.S., and T.S. designed research; M.E., F.v.d.M., J.F., and T.S. performed research; B.S., O.H., and C.S. contributed new reagents/analytic tools; M.E., B.S., and T.S. analyzed data; M.E. and T.S. wrote the paper; B.S. contributed expertise in optical transport (OT) and designed OT analysis workflow; C.S. provided and supervised neuropathology assessment and interpretation; and T.S. supervised X-ray imaging and data analysis.

The authors declare no competing interest.

This article is a PNAS Direct Submission.

This open access article is distributed under Creative Commons Attribution-NonCommercial-NoDerivatives License 4.0 (CC BY-NC-ND).

[1]Deceased September 11, 2020.

[2]To whom correspondence may be addressed. Email: tsaldit@gwdg.de.

This article contains supporting information online at https://www.pnas.org/lookup/suppl/doi:10.1073/pnas.2113835118/-/DCSupplemental.

Published November 24, 2021.

Downloaded from https://www.pnas.org by Niedersaechsische Staats- und Universitaetsbibliothek Goettingen on October 26, 2022 from IP address 134.76.22.130.

fact that this does not require any additional optics between the object and the detector provides a benefit both for dose efficiency and for resolution. Several PC-CT studies have already targeted hippocampal cytoarchitecture in transgenic mouse models for AD (7, 14–17), which exhibit considerable contrast for a typical hallmark associated with this disease, namely β-amyloid plaques. In a recent study, we could also demonstrate the potential of PC-CT on paraffin-embedded hippocampal human tissue affected by AD and evaluate its capability to visualize different pathologies, including plaques, depletion of neurons, or possible recruitment of microglia to affected sites (12).

In this work, we study the 3D cytoarchitecture of the human hippocampus, which serves the formation of declarative long-term memory, i.e., remote episodic or remote semantic memory, but may also affect recent memory, emotions, and vegetative functions (18). Pathologically, the hippocampus is one of the regions first affected in AD (19). As we show here, the throughput of PC-CT measurement, reconstruction, segmentation, and analysis is sufficiently high to treat data from a larger pool, here consisting of postmortem paraffin-embedded tissue blocks of several individuals, both of an AD and of a control group (CTRL), categorized by neuropathological assessment based on the National Institute of Aging – Alzheimer's Association (NIA-AA)–recommended ABC staging (20, 21). We specifically target the dentate gyrus (DG) and its AD-caused structural alterations. As recently shown, hippocampal neurogenesis and plasticity of the entire hippocampal circuitry are linked to the DG and are found to sharply drop in AD (21). Further, we deliberately do not focus on plaques and tangles in AD, which have already been targeted by a high number of studies, but address in particular the nuclear structure of the DG neurons, since recent evidence points to a nuclear origin of AD (22) including chromatin structures (23). In addition, we also include 3D imaging examples of other parts and structures of the hippocampus and provide the corresponding statistical analysis.

Fig. 1 shows a schematic of the hippocampus that is embedded in both left and right temporal lobes of the cerebral cortex, as a part of the limbic system. In Fig. 1*A*, the hippocampus is sketched in the sagittal plane, where it forms an elongated structure of about 4 to 5.2 cm in length (24). In Fig. 1*B*, the frontal plane is shown, in which the appearance is often denoted as snail shaped. Its characteristic functional units are shown in Fig. 1*C*, most prominently including the cornu ammonis (CA) and the DG, which is a dense zone of granule cells. In the polysynaptic signal pathway relevant in semantic memory formation, input signals from the entorhinal cortex (EC) reach first the DG, which is composed of elliptically shaped granular cells with millimeter-long dendrites. Connected through mossy fibers, information is further processed in the CA, whose neurons are characterized by their pyramidal-shaped bodies. The compartmentalization of the CA with commonly attributed subregions CA1 to -4 is not entirely standardized. The information exits the hippocampus to the inferior temporal cortex, the temporal pole, and the prefrontal cortex, constituting the gray matter (GM). There are further pathways of information processing, involving myelinated tracts in the white matter (WM) that link the hippocampus to further brain regions. The physiological relevance of the hippocampus, with respect to several important signal pathways and its pivotal role in memory function and neurodegenerative diseases, in particular in AD, underpins the necessity to study its 3D structure with cellular and subcellular resolution.

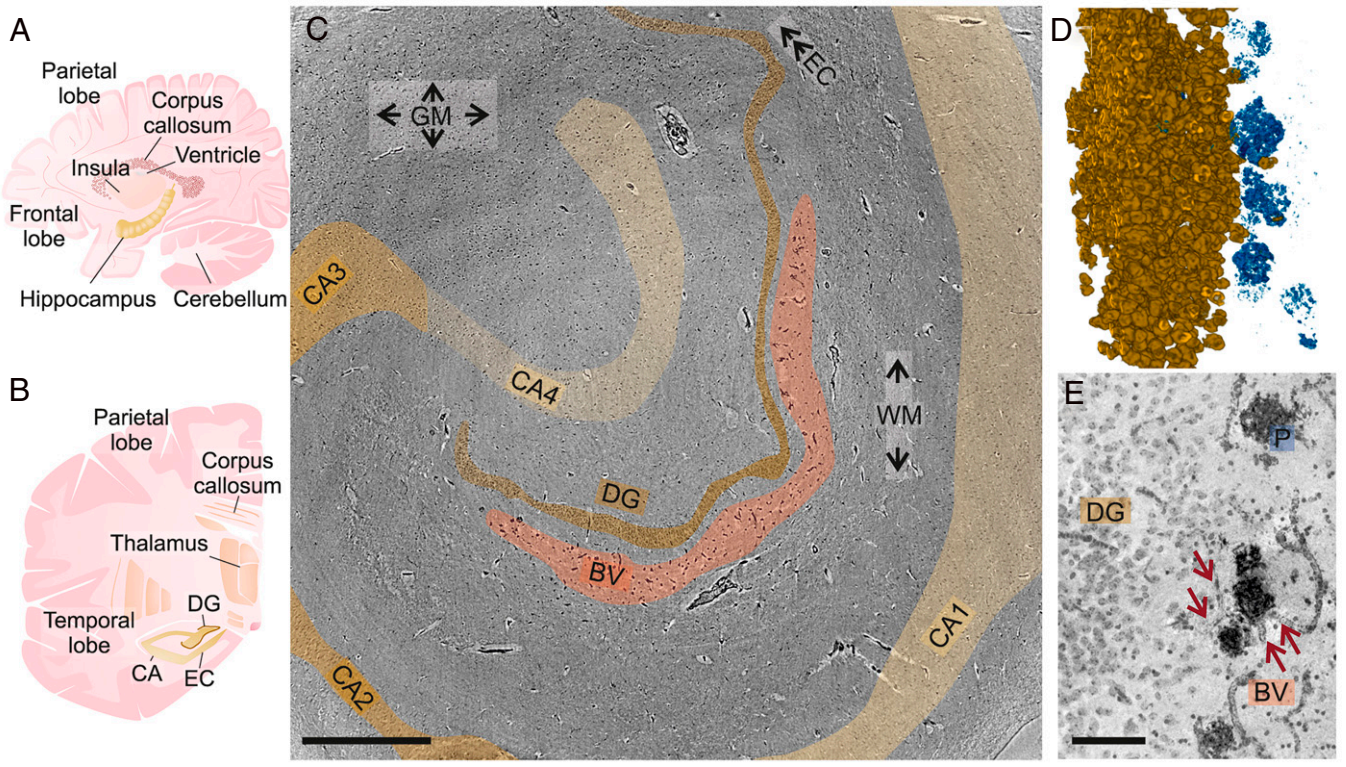

Fig. 1. Human hippocampus overview. (*A* and *B*) Schematics of the human hippocampus (gold) and its location, (*A*) in sagittal and (*B*) in frontal view. (*C*) Virtual slice through overview PC-CT data in EB configuration. The different neuronal layers are outlined: DG; CA differentiated into CA1, CA2, CA3, and CA4; WM; GM; and EC. A region with calcified blood vessels (BV) is also indicated. (*D* and *E*) High-resolution PC-CT data from an AD patient. (*D*) Volume rendering of calcified plaques (blue) in close proximity to the DG (gold). (*E*) Calcified β-amyloid-plaques (P) and calcified BVs are observed only to one side of the DG, as shown here in a maximum-intensity projection (16.2 µm thickness). Red arrows indicate the vascular connections between plaques. (Scale bars: *C*, 1 mm; *E*, 30 µm.)

Downloaded from https://www.pnas.org by Niedersaechsische Staats- und Universitaetsbibliothek Goettingen on October 26, 2022 from IP address 134.76.22.130.

To cover the hippocampal cytoarchitecture in a larger patient cohort, we increase the sample throughput with respect to earlier work (12) by an optimized recording strategy enabling a large sample pool at high and comparable data quality, and we implement a multiscale PC-CT workflow for human brain tissue, based on parallel-beam (PB) recordings at high field of view (FOV) combined with zooms into region of interest (ROI) scanned at high magnification based on cone beam geometry. We then use machine learning based on the V-net architecture to segment neurons, followed by optimal transport (OT) theory to unravel pathological alterations. Note that OT enables us to identify "movement" in a patient cohort based on transport metrics in a structural feature space, which we define in the image segmentation step. OT also offers significant advantages over standard statistical tools such as *t* testing of a single parameter, since it can compare the entire neuron population, by metrics quantifying changes in their distribution.

The implementation of PC-CT, notably regarding the multiscale configuration that comprises different zoom levels, is detailed in *Materials and Methods*. Beginning with overview scans with a FOV of several millimeters in expanded-beam (EB) configuration as in Fig. 1 or in PB, subregions of the hippocampus are presented at the different zoom levels in *Results I: Multiscale Tomography of the Hippocampus*. The structure of granule cell nuclei in the DG is then investigated in volumes of 10^8 to 10^9 μm^3 at voxel size of $px \approx 160$ nm and in some cases even at $px \approx 50$ nm, based on geometric magnification using a divergent and highly coherent beam exiting an X-ray waveguide (WG). In the high-resolution reconstructions, neurons and in particular DG cell nuclei are segmented. Based on the segmentation masks, histograms of morphological features are obtained, containing results on the order of 10,000 neurons for each tissue sample. Histograms of five selected features in autopsies of 20 individuals (11 subjects with intermediate to high AD neuropathologic change according to ref. 20, in the following referred to as AD; 7 controls; and 2 with diffuse presentation based on ABC score) are then compared in *Results II: Geometric and Statistical Analysis*, using the OT tools. In a very general manner, we propose an analysis workflow to identify a pathway from healthy to pathological structure.

Results I: Multiscale Tomography of the Hippocampus

Fig. 1*C* shows the PC-CT result obtained for the largest FOV, covering an 8-mm biopsy punch of a $2 \times 3 \times 0.3$-cm^3 tissue block, scanned in EB configuration (*SI Appendix*, Tables S1 and S2 and Fig. S1). The quintessential structure supporting all further identification of ROIs, as already summarized in the Introduction, is easily recognized and labeled based on visual inspection of the 3D data. Already at this coarse level, the granular cell band of the DG can be identified. It is bordered by a tract of particularly electron-dense blood vessels, indicative of calcifications. Note that calcified vasculature within the hippocampus was frequently observed in tissues of different subjects, both AD and CTRL. As presented in Fig. 1 *D* and *E* for an AD case, these emerge particularly electron dense and may even traverse β-amyloid, which then also show highly elevated electron density (as reported in ref. 12). In addition, other regions such as the pyramidal cell band of the CA, the WM, and the EC can easily be located. Identification of these regions is important in view of subsequent extraction of further subvolumes with a 1-mm biopsy punch for the high-resolution scans. As a proof of principle that these large FOVs can also be scanned with smaller voxel sizes, the full 8-mm punch was further scanned in PB configuration (*SI Appendix*, Table S2). Using dynamic stitching implemented by the NRStitcher (nonrigid stitching of terapixel-scale volumetric images) program (25), 7×7 individual scans were combined to again cover the entire 8-mm punch in a single large volume. By this approach, a tissue volume of 63 mm^3 was covered with submicrometer voxel size. Fig. 2 presents frontal plane slices through the stitched reconstruction volume. In Fig. 2*A*, gray squares mark the single tomograms. With a few local ring artifacts only, structures can be successfully traced throughout the volume, well beyond the boundaries of a single scan. Fig. 2*B* illustrates the winding of the DG band throughout the volume in two different frontal planes. This 3D morphology with its invaginations helps to accommodate a sufficiently high number of DG cells. Based on the large FOV even in a single tomogram, the PB data are particularly suitable to quantify the DG-band morphology and width (see Fig. 3 and further

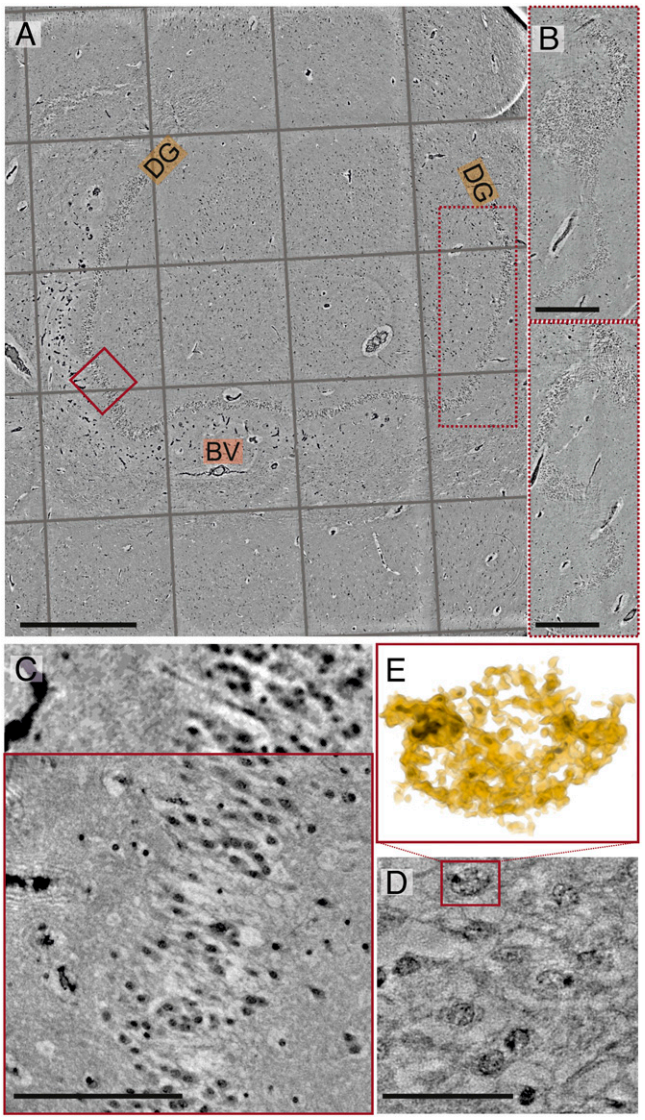

Fig. 2. Multiscale PC-CT data. (*A*) Virtual slice through the stitched reconstruction volume of the entire 8-mm tissue sample obtained from 7×7 scans in PB configuration. Labels indicate the ends of the DG band in this slice, as well as calcified BVs. The red dashed box marks the region that is further detailed in *B*, in two different parallel planes, demonstrating how the DG band winds through the volume. (*C*, *Bottom*) Detailed view of the DG band, as obtained from a CB scan recorded at $M \approx 40$, at the position marked by the solid red square in *A*. For comparison of data quality and contrast, *C*, *Top* shows the corresponding PB data. (*D*) Highest zoom of the DG structure, recorded at $M \approx 130$. The nuclear envelope and heterochromatin become visible by median-filtered maximum-intensity projection over 0.5 μm. (*E*) A single nucleus is further highlighted by a full 3D rendering of the electron density. Note that also here, darker areas are indicative of higher densities. (Scale bars: *A*, 1 mm; *B*, 0.5 mm; *C*, 100 μm; *D*, 30 μm.)

Downloaded from https://www.pnas.org by Niedersaechsische Staats- und Universitaetsbibliothek Goettingen on October 26, 2022 from IP address 134.76.22.130.

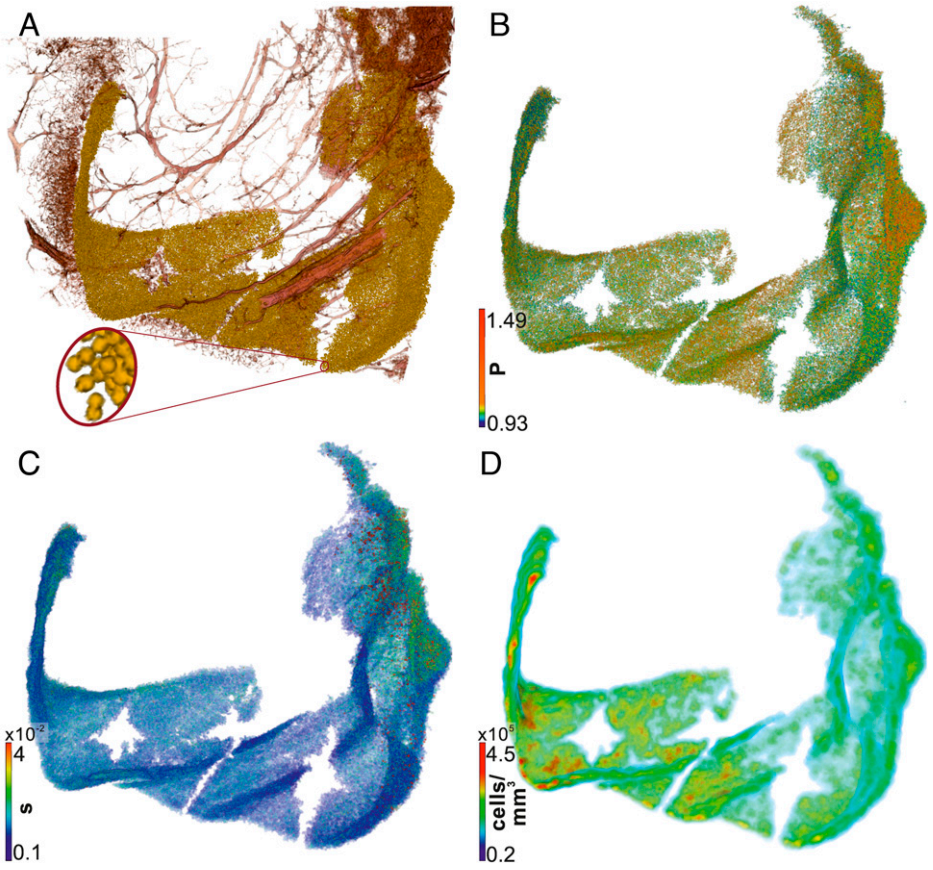

Fig. 3. DG overview. The DG band in a section of 1.25 mm thickness (septotemporal axis) shows (*A*) segmented DG cell nuclei (gold) and vasculature (red) and (*B–D*) rendering in false colors representing (*B*) the normalized electron density P of the nuclei, (*C*) its variance *S*, and (*D*) the local granular cell density.

analysis summarized in *SI Appendix*, Fig. S3 and detailed in the text in *SI Appendix*). To image ROIs at higher magnification $M \simeq 40$ in cone-beam (CB) configuration and without local tomography artifacts, subvolumes were extracted from the 8-mm block using a 1-mm biopsy punch. Fig. 2*C* presents a slice through such a ROI, indicated by a red square in the overview scan. In this configuration, even the substructure of DG cell nuclei can be unveiled. These details are even better resolved by further increasing the geometrical magnification to $M \simeq 130$, as shown in Fig. 2*D* for a slice and in Fig. 2*E* for a 3D volume rendering of a single nucleus, based on its electron density.

Importantly, the image quality allows for semiautomatic segmentation of the granular cell nuclei using the Ilastik software (26) and a subsequent volume rendering of the annotated segmentation masks using Avizo Lite (Thermo Fisher Scientific). Fig. 3 presents an example for a volumetric perspective, showing the overall bent shape of the DG cell band in Fig. 3*A* (gold), jointly with the vasculature (red). Holes in the DG band are due to major blood vessels penetrating the DG. Keeping the perspective, and applying this DG mask to the PC-CT gray values, we can present volume renderings of different quantities: (Fig. 3*B*) normalized electron density P; (Fig. 3*C*) standardized relative variance $S = \sigma^2/\rho^2$ of the electron density within the nuclei, indicative of the prevalence of heterochromatin; and (Fig. 3*D*) the local cell density, averaged within a radius of 50 μm. In this manner, the overall distribution and local inhomogeneities can be visualized.

Next, we further illustrate high-resolution results obtained in CB configuration for the examination of specific regions in the hippocampus such as CA1, DG, surrounding GM, and WM.

Cornu Ammonis 1. Fig. 4 shows exemplary results obtained for the cornu ammonis 1 (CA1) region, for a 1-mm sample that was extracted and scanned as detailed in *SI Appendix*, Table S2. The elongated, pyramidal shape that is typical of neurons in the CA layer is well visualized by the maximum-intensity projections (MIPs) presented in Fig. 4 *A–C*. In each cell, body, nucleus, and nucleolus can be differentiated. For some cells, such as the one marked by the top arrow (Fig. 4*A*), the contrast between cell body and nucleus appears to reflect the position of the nuclear membrane, while for others (Fig. 4*A*, bottom arrow), the dominant effect is an overall increased electron density in the nucleus. Further, the density within the cytosol shows some variation. This is also observed for other cell types, as shown in Fig. 4*B*, depicting the substructure of a satellite cell attached to a neuron. In line with the function of the CA neurons for one-way signal processing throughout the hippocampus, the consistent polarization and orientation with the characteristic long dendrite are very well visible throughout the 3D reconstruction volume. The contrast is sufficient to trace the large dendrites over several tens of micrometers as highlighted in Fig. 4*C*. Using Ilastik, neuronal cell bodies and nuclei are segmented and 3D rendered as shown in Fig. 4 *D–F*.

In the data of Fig. 4 *C* and *E*, areas of lower electron density (light gray values) are often observed around the neurons. To check whether this observation of lower electron density could eventually be an artifact of sample preparation, e.g., by the dehydration-and-embedding procedure of preparing formalin-fixed and paraffin-embedded (FFPE) tissue blocks, we varied the preparation and also scanned the tissue in a hydrated state. For this purpose, a 1-mm sample was taken from a tissue block, which was first chemically fixed with 10% formalin and then

Downloaded from https://www.pnas.org by Niedersaechsische Staats- und Universitaetsbibliothek Goettingen on October 26, 2022 from IP address 134.76.22.130.

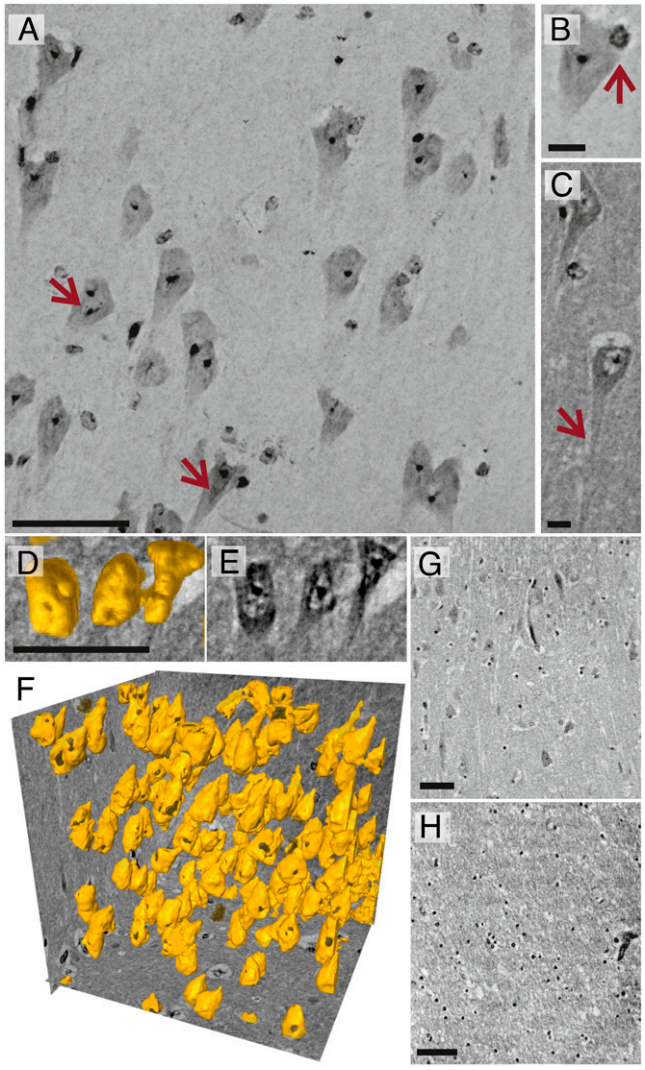

Fig. 4. CA1 region with pyramidal cells (CB data). (*A*) Pyramidal cells with the typical uniaxial orientation are well visualized by their electron density, when gray values are subjected to a MIP, here over a thickness of 13 μm. The contrast is sufficient to distinguish cell bodies and nuclei, either by the visibility of the nuclear envelope (upper arrow) or by an overall increased electron density within the nuclei (lower arrow). (*B* and *C*) MIPs over 8.7 μm thickness. (*B*) Pyramidal cell with a satellite cell attached (arrow). (*C*) Pyramidal cells are branched throughout the volume. (*D* and *E*) Volumetric segmentation of the cell bodies. (*F*) Three-dimensional rendering of the cell bodies (gold) and the nuclei (brown) in the entire reconstruction volume. Gray-scaled orthoslices are included as a support for 3D visualization. (*G*) MIP of gray matter tissue, over 1 μm thickness. (*H*) MIP of white matter tissue, over 1.6 μm thickness. (Scale bars: *A*, *D*, *E*, *G*, and *H*, 50 μm; *B* and *C*, 10 μm.)

stored in phosphate-buffered saline at 4 °C, and examined in its hydrated state, i.e., neither dehydrated nor paraffin embedded. Interestingly, this showed that these areas of decreased electron density are also present in the images of hydrated tissue (*SI Appendix*, Fig. S6).

Segmentation of pyramidal neurons was then applied to tissue samples from different subjects, both of the AD and of the CTRL group. Samples were extracted from the same position in the hippocampus. Note that pathological changes associated with AD are particularly pronounced in this region. Notably, tissue samples from three individuals diagnosed with AD (according to ABC staging; subjects 2, 6, and 21, aged 78 ± 11 y) were compared to four controls (subjects 16, 17, 20, and 21, aged 66 ± 20 y) and a further sample (subject 12). The results are reported in *SI Appendix* and visualized in *SI Appendix*, Fig. S4.

Gray Matter. Fig. 4*G* shows a virtual slice (MIP) through hippocampal GM tissue. For sample collection, the GM region was identified based on histological analysis (stained by hematoxylin and eosin as well as Bielschowsky silver impregnation). Pyramidal cells are also segmented in this region, enabling again the evaluation of neuron density, neuronal morphology, and orientation in full 3D.

White Matter. Fig. 4*H* displays a cross-section through WM tissue. Again, the position at which the sample was extracted by a biopsy punch in the FFPE block was chosen based on evaluation of neighboring histological sections (stained by hematoxylin and eosin as well as Bielschowsky silver impregnation). This tissue segment does not exhibit particular neurons as the CA and GM do, as expected, but appears rather fibrous, reflecting the myelinated fibers of the WM.

Dentate Gyrus. The DG is a particularly substantial component in the information processing within the hippocampus. Fig. 5 shows a reconstruction of this region from data scanned in the CB configuration. As exemplified in Fig. 5*A*, subcellular details can be visualized. The virtual section is in the same plane as in Fig. 2. In Fig. 5*B*, the volume is sectioned in a plane parallel to the DG band, emphasizing its wall-like appearance. Granular cells exhibit a well-structured electron density within their nuclei, which is surrounded by regions of lower electron density (lighter gray values) in the cell body. Even interconnections between single cells can be noticed. The zoom-in highlights the particularly large variance of the electron density distribution in cell nuclei, which can be associated with heterochromatin.

Different features in the reconstruction volume of the DG were then identified and segmented, again using the interactive learning and segmentation toolkit Ilastik. Fig. 5*C* shows the volume-rendered segmentation of DG cell nuclei. Based on the center of mass of the nuclei, a 3D cell density map was computed as shown in Fig. 5*D*. The density obtained from the high-resolution scans in CB configuration confirms the cell density analysis of the large FOV overviews recorded in the PB configuration (Fig. 3*D*). The density ranges between 2 and $4.5 \cdot 10^5$ cells/mm^3, which is in good agreement with the literature (27).

Results II: Geometric and Statistical Analysis

Histograms of Structural Properties of DG Nuclei. As a next step, we quantify the DG cytoarchitecture in 3D to gain an understanding of its intersubject variation both in the healthy physiological state and in the pathological context of AD. To this end, the DG band in samples of 20 different subjects was scanned, reconstructed, segmented, and analyzed. AD cases were identified based on the ABC score (20). Notably, samples from 11 AD subjects aged 76.6 ± 9.3 y, 7 CTRL subjects aged 76.6 ± 7.0 y, and 2 further subjects with no group assignment were collected, as listed in *SI Appendix*, Table S1. Similar to the multiscale workflow described above, 1-mm samples were extracted from each tissue block and imaged first in PB and then in CB configuration. The following analysis is mainly based on the CB data, due to the higher resolution capable of resolving nucleic structures, while the overview scans in PB configuration helped in correct positioning of CB scans and analysis robustness. The analysis of the PB configuration data is given in *SI Appendix*, Fig. S3 and corresponding text sections.

Fig. 6 illustrates the segmentation of DG neuronal nuclei (CB data). In Fig. 6*A*, the same region is shown before and after superimposing the object mask, generated from the segmentation by the machine-learning workflow, described in Fig. 6*C*. For each object in the segmentation output, i.e., from each DG cell nucleus, several structural properties are evaluated for further

Downloaded from https://www.pnas.org by Niedersaechsische Staats- und Universitaetsbibliothek Goettingen on October 26, 2022 from IP address 134.76.22.130.

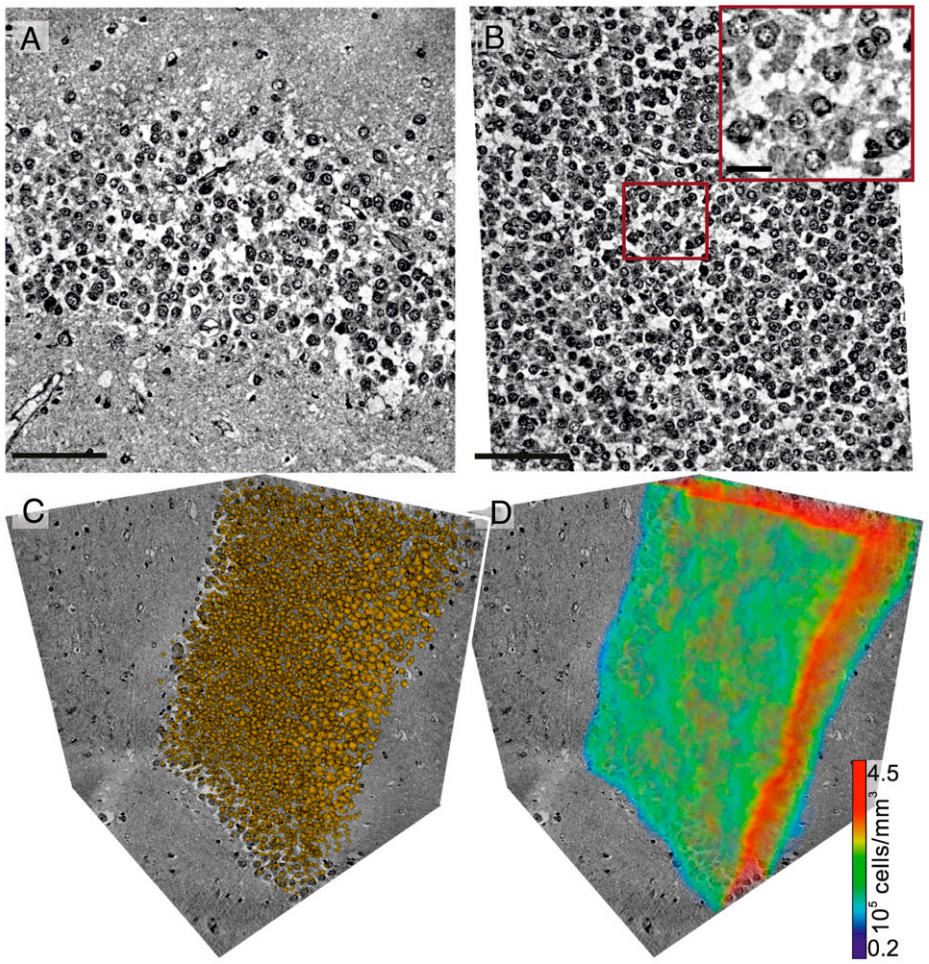

Fig. 5. Zoom into the DG cell band (CB data). (*A*) Transverse slice through the band. (*B*) Slice parallel to the DG band. The red square marks a region that is shown in the zoom and with grayscale chosen to highlight the structure of the nuclei, i.e., the variance of electron density within the nuclei. (*C*) Volume rendering of DG cell bodies. (*D*) Rendering with color indicating the local cell density (see color bar). (Scale bars: *A* and *B*, 100 μm; *B*, *Inset*, 20 μm.)

analysis: 1) median of the electron density ρ (compactness parameter), 2) normalized variance of electron density $s = \sigma^2/\rho^2$ as a proxy for the spatial variations within the nucleus (heterogeneity parameter), 3) nuclei volume v (size parameter), 4) sphericity φ of the nucleus (form parameter), and 5) the number of neighbors *nn* within the local vicinity (neuron packing parameter). Here, object vicinity was defined by a radius given as $\bar{x}_{nn} + 2 \cdot \mathrm{MAD}_x = 13.5$ μm, where $\bar{x}_{nn} = 8.8$ μm denotes the median of the next-neighbor distance distribution of all samples, and $\mathrm{MAD}_x = 3.5$ μm its median absolute deviation. Fig. 6*D* presents the resulting histograms for all five structural features, as the example of one subject belonging to the CTRL group. In this particular case, the histograms contain data corresponding to a total of 3,595 segmented nuclei in the reconstruction volume satisfying the following selection criteria applied to the segmentation output: Only objects with $v > 35$ μm^3, $0.6 \cdot \bar{x}_{nn} < x_{nn} < \bar{x}_{nn} + 3 \cdot \mathrm{MAD}_x$, as well as lying within the 1.5× interquartile range of any of the five features, are considered for statistical evaluation. These criteria have been chosen to minimize bias from segmentation artifacts.

Intersubject Variation and Effects of AD. The segmentation of the granule cell nuclei and extraction of the five parameters per cell, as described above, are then carried out for all individuals, including AD patients and CTRLs, based on the same automated workflow. For each property (parameter) and each individual, an entire histogram containing the data of all segmented granules is available. First, the different properties are compared independently, one by one. Fig. 7 presents results for electron density ρ and the heterogeneity parameter s (see *SI Appendix*, Fig. S2 for all other parameters). The violin plots shown in Fig. 7*A* provide a quick overview and illustrate the degree of intra- and intergroup variations of the histograms. Before addressing these differences at the level of the entire histograms, the median values of the distributions are compared for the two groups (AD and CTRL). The electron density is slightly higher for AD than for CTRL subjects; i.e., $\bar{\rho}_{\mathrm{AD}} = 320.91$ nm^{-3} versus $\bar{\rho}_{\mathrm{CTRL}} = 318.77$ nm^{-3}, with a reduced volume, i.e., $\bar{v}_{\mathrm{AD}} = 101.85$ μm^3 versus $\bar{v}_{\mathrm{CTRL}} = 135.88$ μm^3, both indicating a trend to more compact nuclei, with p values (Welch's t test $p \approx 0.02$ and $p \approx 0.07$ for ρ and v, respectively). At the same time, the median of the heterogeneity parameter s increases from $\bar{s}_{\mathrm{CTRL}} = 1.07 \cdot 10^{-5}$ to $\bar{s}_{\mathrm{AD}} = 1.45 \cdot 10^{-5}$ in CTRL versus AD subjects, indicating a trend toward a more heterogeneous spatial structure of the nucleus in AD, but with $p \approx 0.17$, this difference in median values is not significant. Beyond comparison of the median values, however, entire granule populations should be compared between subjects and groups, which will lead us again to consider the changes in s as relevant to discriminate between pathological and healthy states (see further below). Taking into account the entire neuron population is important, since the physiological functions may require a certain bandwidth of structural parameters, i.e.,

Downloaded from https://www.pnas.org by Niedersaechsische Staats- und Universitaetsbibliothek Goettingen on October 26, 2022 from IP address 134.76.22.130.

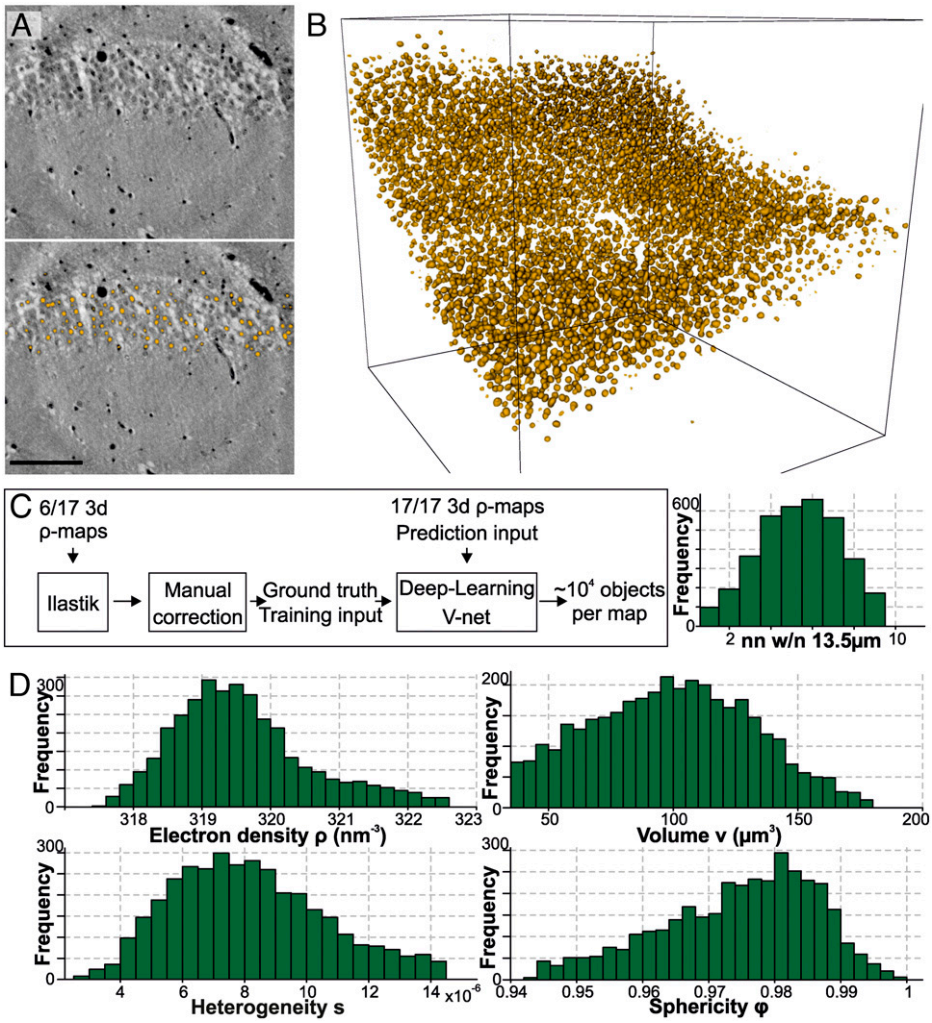

Fig. 6. Segmentation workflow for DG nuclei. (*A*) Slice through exemplary 3D input data (CB configuration), (*Top*) without and (*Bottom*) with mask annotations. (*B*) Three-dimensional rendering of the mask, within a cubic volume of side length 400 μm. (*C*) Flow diagram illustrating the steps of segmentation. (*D*) To each masked object (DG cell nucleus), a number of properties can be attributed, resulting in respective histograms. (Scale bar: 100 μm.)

a dispersion of properties associated with functional states of granules. It is therefore of interest to compare the inter- and intragroup differences also in view of the entire histograms, as quantified by the Wasserstein metric (W). Fig. 7*B* shows a matrix of pairwise differences of the ρ distributions ("distance chart"), evaluated with W. The matrix is divided into four quadrants, showing differences between individuals within and between the groups. Notwithstanding the large variations at the subject level that are highlighted by this display, slightly increased differences can be noted already from visual inspection of the two quadrants comparing subjects across the groups.

To cope with the two major challenges of the data, the strong intersubject variation and the dispersion of neuron structural parameters of any single subject, we adopt a strategy, where each individual is represented by a point cloud in a five-dimensional space of structural parameters, denoted in the following as the feature space. The analysis of the point clouds below is motivated by the fact that intergroup structural differences for corresponding classification of AD and CTRL groups are expected to be better revealed in higher dimensions. Note that only for the special and very unlikely case that the point cloud distribution can be written as a factorized (separated) product to one-dimensional distributions, no information is lost, when treating each dimension separately. Already a simple projection to a two-dimensional subspace, as exemplified in Fig. 7*C*, shows that the point clouds do not separate (factorize), since the structure parameters are weakly correlated.

Classification of AD Pathology vs. Control. The point clouds representing the granule cell population for each subject, as introduced above, are further analyzed in the five-dimensional feature space. First, we standardize the point clouds in each dimension (feature) separately by the population (i.e., the union of all sample point clouds) mean and standard variation. The standardized variables are denoted by the respective capital letter (P, S, V, Φ, NN). Then, each subject's point cloud is approximated by a Gaussian distribution, with mean and covariance matrix given by the empirical mean and covariance matrix of the point cloud. This distribution can be conceptualized as an ellipsoid, centered at the mean, orientation of the principal axes given by the eigenbasis of the covariance matrix and their length by the square root of the corresponding eigenvalues. A natural metric on the set of Gaussian distributions is obtained by combining the Bures metric (28) on the covariance matrices with the Euclidean distance on the mean values. This yields the L^2 OT distance, denoted by $\mathcal{W}$, between the two Gaussian distributions (29), which has recently become increasingly popular in data analysis applications (29, 30).

Downloaded from https://www.pnas.org by Niedersaechsische Staats- und Universitaetsbibliothek Goettingen on October 26, 2022 from IP address 134.76.22.130.

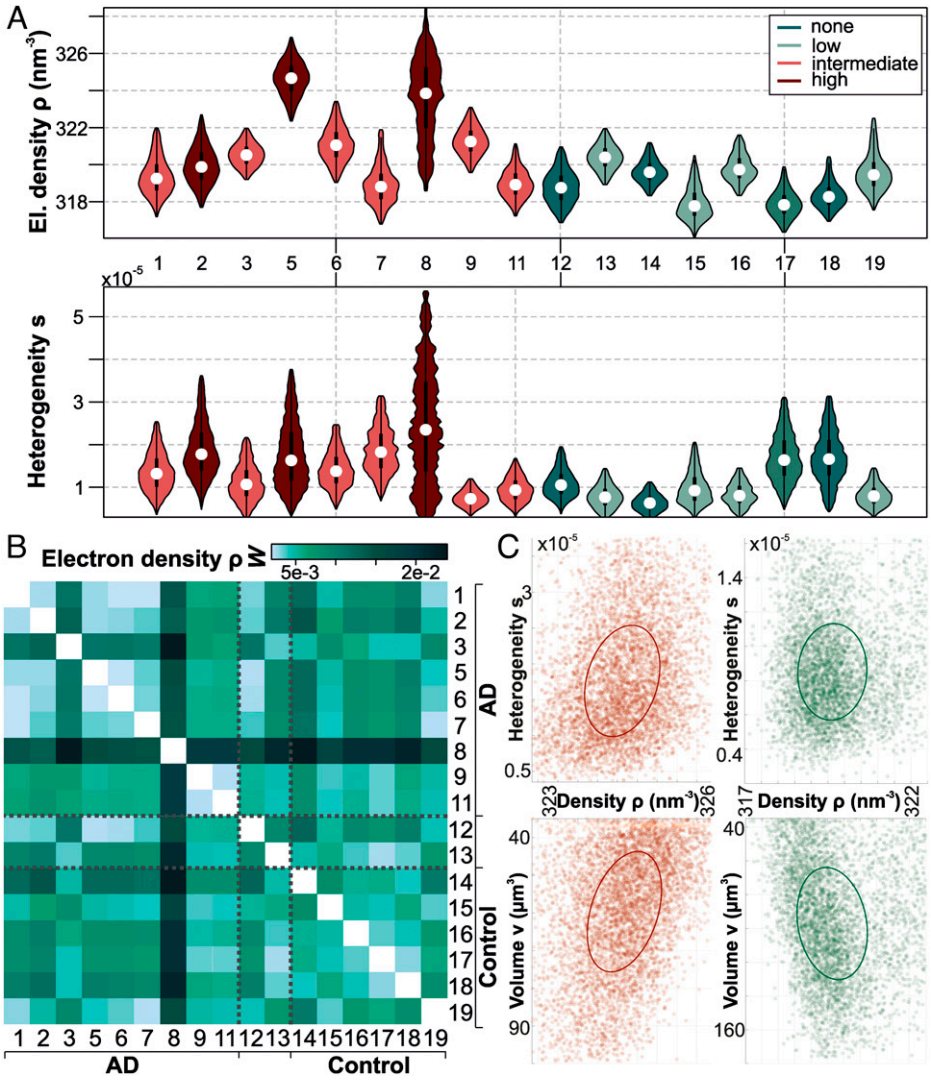

Fig. 7. Structural features of DG cell nuclei. (*A*) Violin plots of electron density ρ and heterogeneity *s*, reflecting the histogram of the selected feature for each individual. The color scheme refers to the ABC score from neuropathological staging. (*B*) Wasserstein metric *W* calculated between any two patients and arranged in a matrix, as a measure of interhistogram distances, here shown for ρ. Gray dashed lines separate groups. (*C*) Point clouds in the feature space, defined here by two selected features, illustrated for the example of two subjects (*Left*, AD group; *Right*, CTRL group), (*Top*) *s* vs. ρ and (*Bottom*) *v* vs. ρ. Each point corresponds to one neuron. Ellipsoids indicate the results of a PCA with half axis defining the principal axis or equivalently the 1σ intervals when fitting a two-dimensional Gaussian distribution to the point cloud.

Fig. 8 reports on the point cloud analysis and the corresponding classification in feature space. In Fig. 8*A*, 2D projections of the Gaussian distributions are visualized as ellipsoids, Fig. 8 *A*, *Left* for the AD group (orange-red) and Fig. 8 *A*, *Right* for the CTRL group (green). The distribution in the V/P plane (Fig. 8 *A*, *Top*) and the S/P plane (Fig. 8 *A*, *Bottom*) shows a larger diversity for the AD group compared to the CTRL group. The visualization of ellipsoids in 2D also serves to illustrate the optimal transport cost: Ellipsoids representing patients 15 and 19, for example, are quite distinct, which is reflected by $\mathcal{W} = 0.86$ (V/P plane) and $\mathcal{W} = 0.74$ (S/P plane), respectively. Contrarily, patients 15 and 12 are closer, evaluating to $\mathcal{W} = 0.21$ (V/P plane) and $\mathcal{W} = 0.29$ (S/P plane), respectively. The distances $\mathcal{W}$ between any two individuals are visualized in the matrix shown in Fig. 8*B*, which can again be considered as a distance chart, now taking into account the full five-dimensionality of the feature space. Darker colors indicate a higher cost (distance) and hence a stronger dissimilarity between the 5D ellipsoids of the corresponding subjects. Two patients stand out strongly: numbers 5 and 8, which are two AD cases in an advanced state (both show an ABC score of "high" and have a distinct high B score compared to one further subject ranked with ABC score of high).

The OT distance $\mathcal{W}$ can also be evaluated directly at the level of point clouds (29), making the Gaussian approximation an optional intermediate step. For the full point clouds one also obtains a distance chart analogous to that in Fig. 8*B*. We perform the subsequent analysis both on full point clouds and with the Gaussian approximation. Every subject can now be interpreted as one point in "subject space" where distances are measured by $\mathcal{W}$ (with or without Gaussian approximation). While this space is not a linear vector space, it has the structure of a Riemannian manifold (intuitively, a curved hypersurface). This manifold can then be approximated locally by its tangent space at a suitable reference point (usually the Riemannian center of mass of the samples) (31). Thus, we have obtained an embedding of the subjects into the linear tangent space (where each individual is represented by one point, which in turn represents a point cloud or a Gaussian distribution on feature space), where we

Downloaded from https://www.pnas.org by Niedersaechsische Staats- und Universitaetsbibliothek Goettingen on October 26, 2022 from IP address 134.76.22.130.

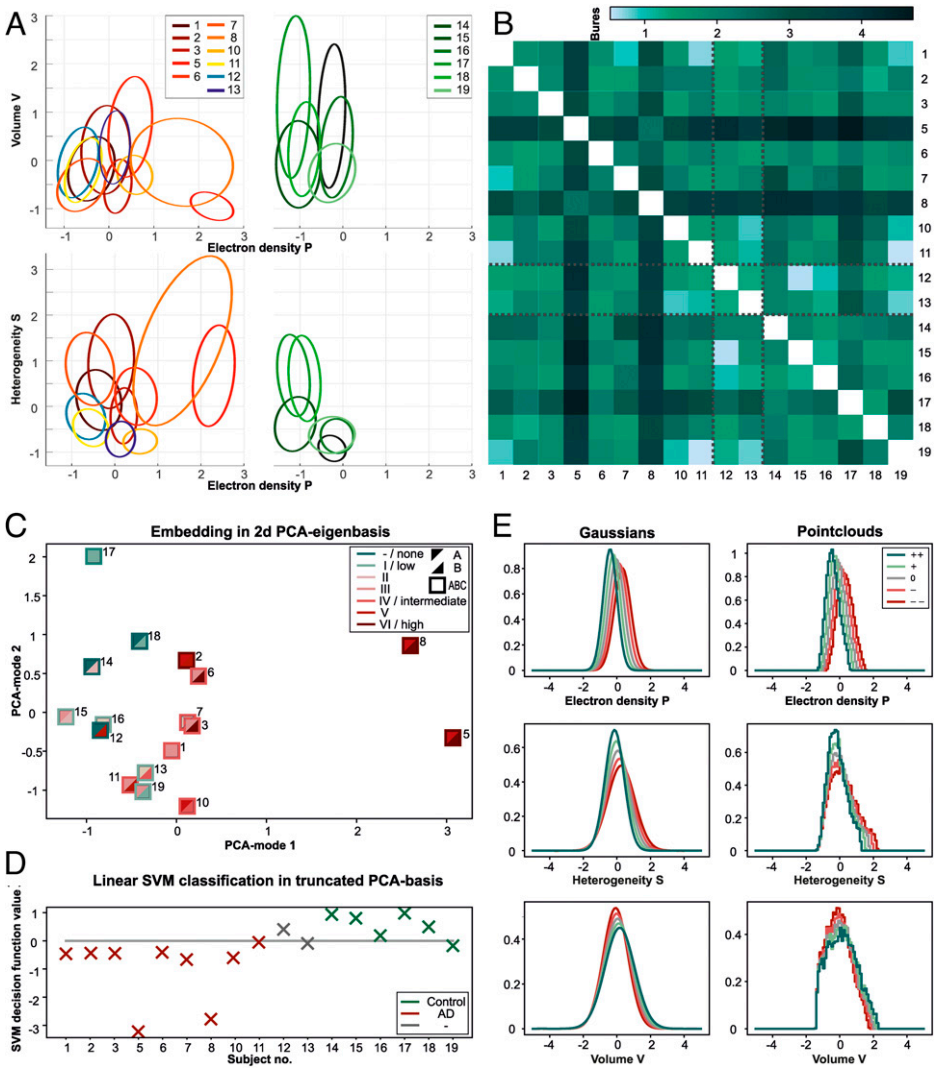

Fig. 8. Multidimensional analysis, optimal transport, and classification. (*A*) Ellipsoidal representations of the DG cell nuclei in selected 2D subspaces of the full 5D feature space. Ellipsoids are shown for 17 different subjects, (*Left*) subjects with AD and with no group assignment and (*Right*) CTRL, showing (*Top*) volume *V* vs. electron density P and (*Bottom*) electron density variance *S* vs. P. (*B*) Matrix plot of the Bures cost (distance chart), with each entry referring to the distance between the respective 5D ellipsoids. With respect to the chosen metric, each subject can be located in a subject space, constructed from the ellipsoids. (*C*) PCA in a suitable tangent plane of this space yields the dominating components, along which the variance between the subjects is maximized. The PCA components represent linear combinations of different features. Data points representing the different subjects are color coded according to Thal phases (upper left triangle), Braak stages (lower right triangle), and ABC score (frame), but this information is not used in the construction of the tangent space. (*D*) Linear SVM analysis applied to the four most dominant PCA components reveals a hyperplane separating both groups. (*E*) The evolution of histograms according to the first PCA mode is found to describe the change from a healthy to a pathological state, indicating the "stereotypical transformation," from CTRL (++) to AD (−−) tissue. The histograms obtained by (*Left*) Gaussian approximation and from (*Right*) a full calculation taking into account every element of the point clouds are found to be in good agreement.

can now apply standard data analysis tools. Principal component analysis (PCA) can be used to identify the most dominant modes (directions) of variation in the subject point cloud (in the tangent space). Fig. 8*C* shows the coordinates of the patients with respect to the two dominant PCA modes ($pca1$,$pca2$). It is important to note that the feature space and its lower-dimensional (truncated) tangent space are implemented without any prior categorization into groups. Instead, the variance in the data itself is used to identify a pathway of maximum changes ($pca1$ mode). Based on the color code of the data points reflecting the ABC staging, we can already visually infer that this pathway also separates the patient groups. To quantify this further, a classification by a linear support vector machine (SVM) is performed, as shown in Fig. 8*D*, using the four most dominant PCA modes, which cover 92.4 or 88.7% of the data variance, in Gaussian approximation or on point clouds, respectively. The normal vector of the separating hyperplane that was obtained by the SVM can be interpreted as the main direction of discrimination between CTRL and AD in tangent space and differs only by 15° from the direction of the $pca1$ mode. The shifts in the feature histograms corresponding to the direction of $pca1$ are shown in Fig. 8*E* for the Gaussian approximation (Fig. 8 *E*, *Left*) and the point clouds (Fig. 8 *E*, *Right*), respectively, with colors indicating the shifts from CTRL group (green) to AD group (red), in a continuous manner. The evolution of the histograms (disease progression) is very similar for Gaussians and point clouds analysis, which can be regarded as a confirmation of validity and robustness. As a result, we can now indicate quintessential changes in the histograms for all features, as we move along the main axis discriminating pathology and control. These changes are (from physiological to pathological

Downloaded from https://www.pnas.org by Niedersaechsische Staats- und Universitaetsbibliothek Goettingen on October 26, 2022 from IP address 134.76.22.130.

end) 1) increased density, 2) increased heterogeneity, and 3) smaller volume of the nuclei.

Discussion

Pathological Progression and Validity of the Analysis. The analysis presented above indicates that with pathological progression from CTRL to AD, DG cell nuclei become more compact (increase of electron density, reduction of volume) and exhibit higher heterogeneity (higher variance of electron density). These findings are revealed by a quantitative workflow that can be summarized as follows: 1) PC-CT of well-controlled regions of the human brain, for a considerable number of individuals; 2) automated segmentation and classification of many neurons based on machine learning and extraction of structural properties; 3) creation of a "feature space" based on single-cell properties and the neuron population for each individual (one point in the feature space corresponds to a single cell and a point cloud to one patient); and 4) construction of a subject space based on the point clouds and their distances, as quantified by OT theory, and subsequent local linearization, PCA, and SVM analysis. In the subject space, a point corresponds to a single patient and a point cloud to one group. Geometric analysis of the respective subject groups indicates the dominating "modes," which encode a movement of cells in feature space that may correspond to the progression from physiological to pathological states. Since the full OT analysis is numerically complex and relies on very recent mathematical work, we have also implemented a more conservative Gaussian approximation of the point clouds, which provides a fully established and numerically low-cost alternative to the full analysis. Importantly, the Gaussian approximation and the findings on point clouds are consistent, proving that the conclusions are robust with respect to smaller variations in the point distributions. At the same time, Fig. 8*E* shows that the prototypical change of a histogram for the heterogeneity S trends toward an asymmetric distribution for strong AD when estimated on the point clouds. In particular, the distribution exhibits a shoulder toward higher heterogeneity values, hinting at a subpopulation of DG neurons relevant in the pathology. In the Gaussian framework, this detail cannot be captured completely, but appears only as a broadening of the histogram. This nicely illustrates the more complete description provided by OT on the full point cloud.

Heterogeneity, Chromatin, and AD. Next, we raise the question of interpretation of these findings in the context of the aging brain and AD. We have to address in particular the increasing compactness and heterogeneity of the DG cell nuclei, which were identified as a major marker for AD progression by the analysis. Note that OT is able to detect changes in a structural feature such as nuclear volume v, density ρ, or heterogeneity s also in cases where the average parameter—i.e., averaged over the neuron population of a patient—does not change significantly between groups, as tested by a t test for example. This is because OT provides a measure for changes in the entire neuron population and hence also takes into account a change in the distribution such as the broadening observed in Fig. 8*E*. The observed changes in heterogeneity can be interpreted based on Fig. 2 *D* and *E*, where we can recognize the typical structural patterns of heterochromatin as the dominating contribution to the variance of electron density, i.e., the heterogeneity S. This identification is plausible, since the noise contribution to S has been minimized by median filtering prior to the quantification of P and S. The attribution of s to heterochromatin patterns is also in agreement with chromosomal conformation studies by soft X-ray absorption tomography (32). Hence, it is reasonable to draw the conclusion that the increase in heterogeneity is explained by an increasing ratio of heterochromatin to euchromatin or more generally changes in chromatin conformation. In fact, the percentage of DNA in the euchromatin state is smaller in AD than in healthy tissue, as known from fractionation of DNA extracted from postmortem brains (33). By PC-CT subnuclear structure can be assessed at the single-neuron level in larger volumes of human brain tissue without slicing or staining. Currently, the topic of nuclear structure and AD receives much attention as chromatin organization has now been linked to dysregulation of genome architecture in aging and AD brain tissue (23). Further, a nuclear origin of AD and dominant roles of nuclear tau protein and of nuclear lamins have been pointed out (34). A specific contribution to the increased level of heterogeneity that we observe here could also be due to the formation of distinct heterochromatic structures designated as senescence-associated heterochromatic foci (SAHF). SAHF have first been reported for senescent human fibroblasts (35) and have been described as subnuclear heterochromatic compartments, which potentially silence genes that promote cell cycle progression (36). More recently, SAHF formation and senescence have also been discussed in neurons and glial cells with respect to a putative role in AD (37). An additional factor to the observed heterogeneity could be the nucleoplasmic reticulum that interrupts the smooth nuclear surface by tubular invaginations of the nuclear envelope and for which a significant expansion was reported in AD brain tissue (38), resulting from neurodegenerative laminopathy.

Structural Variability. After discussing nucleic structure in view of a possible role in AD, we briefly address DG and hippocampal structure in a general context, in view of the average structural parameters and their intersubject variability, also in the physiological regime. To this end, we have evaluated the average neuron density $\bar{\rho}_n$, the local density fluctuations ζ_n as an indicator for possible local defects, the average width of the DG band d_{DG}, and the next-neighbor distance d_{NN}. Note that d_{NN} was quantified from the inverse of the peak position of the structure factor, which was computed from the nuclei center-of-mass positions (*SI Appendix*, *Methods*, *Short-range order of DG-granular cells*). The results are summarized in Table 1. Two observations are noteworthy: First, in contrast to the nucleic structure, the overall spatial distribution of DG neurons in terms of density, density fluctuations, and packing does not differ between groups (AD and CTRL), but was found to differ significantly between subjects. As a result of this study, we can now give accurate numbers for the structure of the human DG, notably its width $d_{\mathrm{DG}} = 32.8$ μm, neuron density $\bar{\rho}_n = 2.32 \cdot 10^5$ 1/mm^3, and the next-neighbor distance $d_{\mathrm{NN}} = 14.29$ μm. In addition, we can quantify the intersubject variance of these quantities. Defining the structural polydispersity for a structural parameter p as $P = \Delta p/p$, we find a surprisingly large value $P = 26\%$ for the width of the DG band, while for neuron density and next-neighbor distance we have $P = 16\%$ and $P = 7\%$, respectively.

Accessibility and Scalability of PC-CT. Finally, we provide a brief note on the accessibility, scalability, and possible translation of PC-CT. The capabilities of PC-CT are currently substantially augmented, both in quantity and in quality, at almost all synchrotron radiation (SR) sources worldwide. Upgrades of electron storage ring and X-ray optics, in combination with dedicated beamlines designed for fully robotic sample handling and automated reconstruction, will substantially increase resolution, image quality, and sample throughput. Furthermore, the current pandemic is catalyzing mail-in and remote beamtime operation. At the same time, ongoing instrumental progress enables at least partial translation of the method from SR to compact laboratory μ-CT, compatible with clinical use, e.g., in the neuropathology units of university medical centers. Both developments will require or can at least significantly benefit from optimized PC-CT reconstruction, segmentation based on machine learning, and data analysis based on OT, as demonstrated here.

Downloaded from https://www.pnas.org by Niedersaechsische Staats- und Universitaetsbibliothek Goettingen on October 26, 2022 from IP address 134.76.22.130.

Table 1. Structural parameters of the DG cell band: mean and SD (All, AD, CTRL)

Parameter (median over subject Neuron population)	All		AD		CTRL		p^*
	Mean	SD	Mean	SD	Mean	SD	
Electron density ρ (1/nm^3)	320.06	2.00	320.91	2.10	318.77	0.92	0.020
Heterogeneity s ($\cdot 10^{-5}$)	1.30	0.50	1.45	0.50	1.07	0.45	0.165
Volume v (μm^3)	115.46	34.26	101.85	28.31	135.88	34.21	0.073
Sphericity φ	0.950	0.016	0.963	0.015	0.954	0.017	0.278
nn within radius of 13.5 μm	4.93	1.39	5.44	1.42	4.17	0.983	0.061
Cell density $\bar{\rho}_n$ ($\cdot 10^5$ 1/mm^3)	2.32	0.37	2.35	0.46	2.32	0.15	0.842
DG bandwidth d_{DG} (μm)	32.82	8.44	34.27	9.04	30.54	7.47	0.358
Next-neighbor distance d_{NN} (μm)	14.29	1.01	13.88	0.95	15.04	0.65	0.009
nn within radius of 13.5 μm	4.83	1.47	5.18	1.66	4.29	0.95	0.166

The upper part refers to CB data and the lower part to PB data. For each subject, the median of the neuron population was calculated. p values reflect group differences only with respect to the parameter median, not the entire neuron population, which is probed by OT. d_{NN} is derived from the structure factor maximum. The evaluation of the parameters is detailed in *SI Appendix, Methods, Structural parameters of DG-cell nuclei*. NN, number of neighbors. $^*t$ test (Welch).

Materials and Methods

Sample Collection and Preparation. Human hippocampus tissue was retrieved at routine autopsy in agreement with the ethics committee of the University Medical Center Göttingen. Following the protocol from clinical pathology routine, autopsy dissection blocks from 23 subjects were 10% paraformaldehyde fixed, dehydrated, and paraffin embedded (FFPE). One FFPE block measures about $2 \times 3 \times 0.3$ cm^3. Following ref. 20, we then classified subjects according to the ABC score, accounting for (A) β-amyloid plaques according to Thal phases (39), (B) neurofibrillar tangles according to Braak stages (19, 40), and (C) neuritic plaques according to the CERAD (consortium to establish a registry for Alzheimer's disease) score (41). Again following ref. 20, subjects with an AD likelihood "intermediate" or "high" according to the compound ABC score were classified as AD (11/20 subjects; 2/11 subject datasets were excluded from CB analysis, as detailed in *SI Appendix, Sample collection and preparation*). Subjects with an AD likelihood "none" or "low" were classified as controls (7/20 subjects; 1/7 datasets were excluded from CB analysis, for the same reason as above). For each subject analyzed in *Results II: Geometric and Statistical Analysis*, the neuropathological findings are listed in *SI Appendix*, Table S1. Note that 2/20 subjects were not assigned to any group due to their diffuse presentation in A, B, and C scores (subjects 12 and 13). For PC-CT analysis, cylindrical samples were then extracted from the FFPE blocks using either a 1- or an 8-mm biopsy punch and inserted into polyimide tubes.

Experimental Setup. The data presented in this work were recorded at the GINIX holo-tomography endstation of the P10 undulator beamline, Petra III, DESY, Hamburg, Germany (42), at a photon energy of 8.0 or 13.8 keV, selected by a Si(111) channel-cut monochromator. To cover the cytoarchitecture over a wide range of length scales, ranging from entire hippocampus structure in the frontal plane down to ROIs within the dentate gyrus at subcellular resolution, the instrument's multiscale capability was used (13), comprising three different optical configurations. First, large FOVs up to about 8 mm were scanned in a beam that was focused by a Kirkpatrick–Baez (KB)-mirror system and subsequently broadened by its divergence. This is denoted as EB configuration. Second, intermediate FOVs up to about 1.5 mm were scanned in a PB configuration, after moving the mirrors out of the beam path. Finally, small FOVs up to about 0.4 mm were scanned at highest resolution, using a compound optics of KB mirrors and X-ray WGs (CB configuration) (10, 43). By adjusting the distance z_{01} between WG and sample, two different voxel sizes of px $\simeq$ 160 nm and px $\simeq$ 50 nm were chosen in this configuration, providing further zoom. The different configurations and parameters are further detailed in *SI Appendix, Methods*.

Reconstruction. Projections were first corrected for empty beam and dark images, recorded before and after the tomography scans. Phase retrieval was performed by either the linearized contrast-transfer function (CTF) scheme or the nonlinear Tikhonov (NLT) algorithm (44). Both are well suited for the holographic regime corresponding to image formation at small Fresnel numbers $F = \frac{\text{px}^2}{z_{\text{eff}}\lambda} \ll 1$, with wavelength λ, and the effective propagation distance $z_{\text{eff}} = z_{12}/M$. After phase retrieval of the projections, tomographic reconstruction was performed by filtered back projection (FBP) or a cone-beam (FDK; Feldkamp–Davis–Kress) algorithm, both as implemented in the ASTRA toolbox (45). Spatial resolution was determined using Fourier shell correlation (FSC), after applying a Kaiser–Bessel window of 7 pixels and a half-bit threshold. Based on the image quality metrics, 2/11 AD and 1/7 control CB datasets were excluded from the analysis to keep the segmentation quality on a similar level for all datasets. Further details are given in *SI Appendix, Methods*.

Segmentation of DG Cell Nuclei. For the PB data, segmentation of DG cell nuclei was carried out using the Blobfinder tool of the segmentation and visualization package Arivis (Arivis AG). The CB data were segmented with the interactive software package Ilastik (26) and a further manual optimization based on image filters and object removal based on visual control. These segmentations served as ground-truth input for machine learning based on convolutional neural networks (CNN) implemented via the Deep-learning V-net, which is the three-dimensional generalization of the U-net design (46), as detailed in *SI Appendix, Methods, Segmentation of DG-cell nuclei*.

Structural Parameters of DG Cell Nuclei. For segmented nuclei of the DG cells, five features were selected for further analysis and computed based on the segmentation mask for each individual: median (over DG neurons) of the nuclear electron density ρ, normalized nuclear electron density variance $s = \sigma^2/\overline{\rho}^2$ (heterogeneity parameter), nuclear volume v, nuclear sphericity φ (shape parameter), and number of neighbors *nn* in a radius of 13.5 μm, a value selected in between first and second coordination shells of the pair correlation function $g(r)$ (10). The pairwise similarity (or equivalently distance) between the one-dimensional histograms (separately foreach feature, Fig. 7) was computed using the Wasserstein metric W of order $p = 2$, as implemented in ref. 47.

Analysis Based on Optimal Transport. In the Gaussian approximation each individual is represented by a normal distribution $\mathcal{N}(\Sigma, \mu)$ with covariance matrix Σ and mean μ. The Bures metric between two covariance matrices was used as in ref. 28 to construct an optimal transport map between the multidimensional normal distributions fitted to the point cloud data. Beyond this Gaussian approximation, point cloud optimal transport plans were also computed with entropic regularization and the Sinkhorn algorithm. Local linearization of the optimal transport metric is performed as described in ref. 31, including the approximate extraction of an optimal transport map from the optimal transport plan between two point clouds. In the Gaussian approximation, the optimal transport center of mass ("barycenter") was used as a reference for linearization, which can be computed efficiently with the fixed-point algorithm of ref. 48 and also serves as a basis to sample 10^4 points from Gaussian distribution for point cloud analysis. Linear SVM classification was performed with the implementation of ref. 49. Full details are given in *SI Appendix, Methods, Analysis based on optimal transport*.

Data Availability. CT reconstructions data have been deposited in Zenodo DOI: 10.5281/zenodo.5658994 (50). All study data are available upon request.

ACKNOWLEDGMENTS. We thank Michael Sprung, Markus Osterhoff, and Bastian Hartmann for support at GINIX and Thomas Jentschke and Jakob Frost for help with segmentation. Support by the Deutsche Forschungsgemeinschaft (DFG) (German Research Foundation) under Germany's Excellence Strategy—EXC 2067/1-390729940 Multiscale Bioimaging—and the German Federal Ministry of Education and Research through Grant 05K19MG2 NeuroTomo is gratefully acknowledged. J.F. and C.S. acknowledge funding by DFG (TRR274-1) and the associated clinician scientist program.

Downloaded from https://www.pnas.org by Niedersaechsische Staats- und Universitaetsbibliothek Goettingen on October 26, 2022 from IP address 134.76.22.130.

1. K. Amunts, K. Zilles, Architectonic mapping of the human brain beyond Brodmann. *Neuron* **88**, 1086–1107 (2015).
2. K. Amunts *et al.*, Interoperable atlases of the human brain. *Neuroimage* **99**, 525–532 (2014).
3. D. H. Adler *et al.*, Characterizing the human hippocampus in aging and Alzheimer's disease using a computational atlas derived from ex vivo MRI and histology. *Proc. Natl. Acad. Sci. U.S.A.* **115**, 4252–4257 (2018).
4. M. Töpperwien *et al.*, Three-dimensional mouse brain cytoarchitecture revealed by laboratory-based x-ray phase-contrast tomography. *Sci. Rep.* **7**, 42847 (2017).
5. E. L. Dyer *et al.*, Quantifying mesoscale neuroanatomy using X-ray microtomography. *eNeuro* **4**, ENEURO.0195-17.2017 (2017).
6. L. C. P. Croton *et al.*, In situ phase contrast X-ray brain CT. *Sci. Rep.* **8**, 11412 (2018).
7. L. Massimi *et al.*, Exploring Alzheimer's disease mouse brain through X-ray phase contrast tomography: From the cell to the organ. *Neuroimage* **184**, 490–495 (2019).
8. A. T. Kuan *et al.*, Dense neuronal reconstruction through X-ray holographic nanotomography. *Nat. Neurosci.* **23**, 1637–1643 (2020).
9. S. E. Hieber *et al.*, Tomographic brain imaging with nucleolar detail and automatic cell counting. *Sci. Rep.* **6**, 32156 (2016).
10. M. Töpperwien, F. van der Meer, C. Stadelmann, T. Salditt, Three-dimensional virtual histology of human cerebellum by X-ray phase-contrast tomography. *Proc. Natl. Acad. Sci. U.S.A.* **115**, 6940–6945 (2018).
11. A. Khimchenko *et al.*, Hard x-ray nanoholotomography: Large-scale, label-free, 3d neuroimaging beyond optical limit. *Adv. Sci. (Weinh.)* **5**, 1700694 (2018).
12. M. Töpperwien, F. van der Meer, C. Stadelmann, T. Salditt, Correlative x-ray phase-contrast tomography and histology of human brain tissue affected by Alzheimer's disease. *Neuroimage* **210**, 116523 (2020).
13. J. Frohn *et al.*, 3D virtual histology of human pancreatic tissue by multiscale phase-contrast X-ray tomography. *J. Synchrotron Radiat.* **27**, 1707–1719 (2020).
14. K. Noda-Saita *et al.*, Quantitative analysis of amyloid plaques in a mouse model of Alzheimer's disease by phase-contrast X-ray computed tomography. *Neuroscience* **138**, 1205–1213 (2006).
15. D. M. Connor *et al.*, Computed tomography of amyloid plaques in a mouse model of Alzheimer's disease using diffraction enhanced imaging. *Neuroimage* **46**, 908–914 (2009).
16. B. R. Pinzer *et al.*, Imaging brain amyloid deposition using grating-based differential phase contrast tomography. *Neuroimage* **61**, 1336–1346 (2012).
17. A. Astolfo, A. Lathuilière, V. Laversenne, B. Schneider, M. Stampanoni, Amyloid-β plaque deposition measured using propagation-based X-ray phase contrast CT imaging. *J. Synchrotron Radiat.* **23**, 813–819 (2016).
18. L. R. Squire, Memory and the hippocampus: A synthesis from findings with rats, monkeys, and humans. *Psychol. Rev.* **99**, 195–231 (1992).
19. H. Braak, E. Braak, Neuropathological stageing of Alzheimer-related changes. *Acta Neuropathol.* **82**, 239–259 (1991).
20. T. J. Montine *et al.*, National Institute on Aging-Alzheimer's Association guidelines for the neuropathologic assessment of Alzheimer's disease: A practical approach. *Acta Neuropathol.* **123**, 1–11 (2012).
21. E. P. Moreno-Jiménez *et al.*, Adult hippocampal neurogenesis is abundant in neurologically healthy subjects and drops sharply in patients with Alzheimer's disease. *Nat. Med.* **25**, 554–560 (2019).
22. L. Gil, S. A. Niño, G. Capdeville, M. E. Jiménez-Capdeville, Aging and Alzheimer's disease connection: Nuclear Tau and lamin A. *Neurosci. Lett.* **749**, 135741 (2021).
23. W. Winick-Ng, R. J. Rylett, Into the fourth dimension: Dysregulation of genome architecture in aging and Alzheimer's disease. *Front. Mol. Neurosci.* **11**, 60 (2018).
24. T. L. McHugh *et al.*, Hippocampal volume and shape analysis in an older adult population. *Clin. Neuropsychol.* **21**, 130–145 (2007).
25. A. Miettinen, I. V. Oikonomidis, A. Bonnin, M. Stampanoni, NRStitcher: Non-rigid stitching of terapixel-scale volumetric images. *Bioinformatics* **35**, 5290–5297 (2019).
26. S. Berg *et al.*, Ilastik: Interactive machine learning for (bio)image analysis. *Nat. Methods* **16**, 1226–1232 (2019).
27. M. Boldrini *et al.*, Hippocampal granule neuron number and dentate gyrus volume in antidepressant-treated and untreated major depression. *Neuropsychopharmacology* **38**, 1068–1077 (2013).
28. P. J. Forrester, M. Kieburg, Relating the Bures measure to the Cauchy two-matrix model. *Commun. Math. Phys.* **342**, 151–187 (2016).
29. G. Peyré *et al.*, Computational optimal transport: With applications to data science. *Found. Trends Mach. Learn.* **11**, 355–607 (2019).
30. F. Santambrogio, "Optimal transport for applied mathematicians" in *Progress in Nonlinear Differential Equations and Their Applications* (Birkhäuser, Boston, MA, 2015), **vol. 87**.
31. W. Wang, D. Slepčev, S. Basu, J. A. Ozolek, G. K. Rohde, A linear optimal transportation framework for quantifying and visualizing variations in sets of images. *Int. J. Comput. Vis.* **101**, 254–269 (2013).
32. M. A. Le Gros *et al.*, Soft x-ray tomography reveals gradual chromatin compaction and reorganization during neurogenesis in vivo. *Cell Rep.* **17**, 2125–2136 (2016).
33. D. R. Crapper, S. Quittkat, U. de Boni, Altered chromatin conformation in Alzheimer's disease. *Brain* **102**, 483–495 (1979).
34. L. Gil *et al.*, Perinuclear lamin A and nucleoplasmic lamin B2 characterize two types of hippocampal neurons through Alzheimer's disease progression. *Int. J. Mol. Sci.* **21**, 1841 (2020).
35. M. Narita *et al.*, Rb-mediated heterochromatin formation and silencing of E2F target genes during cellular senescence. *Cell* **113**, 703–716 (2003).
36. S. Castro-Obregón, Lamin B receptor: Role on chromatin structure, cellular senescence and possibly aging. *Biochem. J.* **477**, 2715–2720 (2020).
37. M. Kritsilis *et al.*, Ageing, cellular senescence and neurodegenerative disease. *Int. J. Mol. Sci.* **19**, 2937 (2018).
38. B. Frost, Alzheimer's disease: An acquired neurodegenerative laminopathy. *Nucleus* **7**, 275–283 (2016).
39. D. R. Thal, U. Rüb, M. Orantes, H. Braak, Phases of A beta-deposition in the human brain and its relevance for the development of AD. *Neurology* **58**, 1791–1800 (2002).
40. H. Braak, I. Alafuzoff, T. Arzberger, H. Kretzschmar, K. Del Tredici, Staging of Alzheimer disease-associated neurofibrillary pathology using paraffin sections and immunocytochemistry. *Acta Neuropathol.* **112**, 389–404 (2006).
41. S. S. Mirra *et al.*, The consortium to establish a registry for Alzheimer's disease (CERAD): Part II. Standardization of the neuropathologic assessment of Alzheimer's disease. *Neurology* **41**, 479–486 (1991).
42. T. Salditt *et al.*, Compound focusing mirror and X-ray waveguide optics for coherent imaging and nano-diffraction. *J. Synchrotron Radiat.* **22**, 867–878 (2015).
43. M. Bartels, M. Krenkel, J. Haber, R. N. Wilke, T. Salditt, X-ray holographic imaging of hydrated biological cells in solution. *Phys. Rev. Lett.* **114**, 048103 (2015).
44. L. M. Lohse *et al.*, A phase-retrieval toolbox for X-ray holography and tomography. *J. Synchrotron Radiat.* **27**, 852–859 (2020).
45. W. van Aarle *et al.*, Fast and flexible X-ray tomography using the ASTRA toolbox. *Opt. Express.* **24**, 25129–25147 (2016).
46. O. Ronneberger, P. Fischer, T. Brox, "U-net: Convolutional networks for biomedical image segmentation" in *Medical Image Computing and Computer-Assisted Intervention–MICCAI 2015*, N. Navab, J. Hornegger, W. M. Wells, A. F. Frangi, Eds. (Springer International Publishing, Cham, Switzerland, 2015), pp. 234–241.
47. D Schuhmacher *et al.*, *Transport: Computation of Optimal Transport Plans and Wasserstein Distances*, R package version 0.12-2 (CRAN, Göttingen, 2020). https:// cran.r-project.org/web/packages/transport/index.html. Accessed 18 November 2021.
48. P. C. Álvarez-Esteban, E. del Barrio, J. Cuesta-Albertos, C. Matrán, A fixed-point approach to barycenters in Wasserstein space. *J. Math. Anal. Appl.* **441**, 744–762 (2016).
49. F. Pedregosa *et al.*, Scikit-learn: Machine learning in Python. *J. Mach. Learn. Res.* **12**, 2825–2830 (2011).
50. M. Eckermann, T. Salditt, Three-dimensional virtual histology of the human hippocampus based on phase-contrast computed tomography. Zenodo. https://zenodo.org/record/5658994#.YZKJWXso_mF. Deposited 16 November 2021.

Downloaded from https://www.pnas.org by Niedersaechsische Staats- und Universitaetsbibliothek Goettingen on October 26, 2022 from IP address 134.76.22.130.